Submitted to

International Europhysics Conference on High Energy Physics, EPS03, July 17-23, 2003, Aachen
(Abstract **092** Parallel Session **5**)

XXI International Symposium on Lepton and Photon Interactions, LP03, August 11-16, 2003, Fermilab

www-h1.desy.de/h1/www/publications/conf/conf_list.html

Elastic Electroproduction of ρ Mesons at High Q^2 at HERA

H1 Collaboration

Abstract

The elastic electroproduction of ρ mesons is studied at HERA with the H1 detector in the kinematic range $8 < Q^2 < 60\ \mathrm{GeV}^2$, $40 < W < 180$ GeV and $|t| < 0.5\ \mathrm{GeV}^2$. The luminosity of 42.4 pb^{-1} gives access to the Q^2 domain where perturbative QCD is expected to apply. The cross section has been measured as a function of Q^2, W and t. The W dependence of the $\gamma^* p \to \rho p$ cross section is observed to become stronger with increasing Q^2, changing from a behaviour compatible with soft Pomeron exchange at low Q^2 to a hard dependence at large Q^2. Spin density matrix elements are measured as a function of Q^2, W and t. Significant t dependent violations of s-channel helicity conservation are observed.

1 Introduction

The subject of this paper is the study of the elastic electroproduction of ρ mesons in ep scattering at high energy:

$$e + p \rightarrow e + \rho + p \;\; ; \quad \rho \rightarrow \pi^+\pi^- . \tag{1}$$

The scattered proton can also be excited into a system Y of mass M_Y which is much lower than the photon–proton centre of mass energy W (“proton dissociative” scattering), this process being the dominant background contribution.

The kinematic domain of the measurement is restricted to:

$$\begin{aligned} 8 < & \;\; Q^2 & < 60\ \mathrm{GeV}^2 \\ 40 < & \;\; W & < 180\ \mathrm{GeV} \\ 0 < & \;\; |t| & < 0.5\ \mathrm{GeV}^2, \end{aligned} \tag{2}$$

where Q^2 is the modulus of the intermediate photon four-momentum squared, W is the hadronic centre of mass energy and t is the square of the four-momentum transfer to the proton.

At low Q^2, the $\gamma^* p \rightarrow \rho p$ cross section is characterized by a “soft” energy dependence which can be seen as due to pomeron ($I\!P$) exchange with $\mathrm{d}\sigma/\mathrm{d}t \propto W^{4(\alpha_{I\!P}(t)-1)}$, where the soft pomeron trajectory is parametrized [1] as $\alpha_{I\!P}(t) = \alpha_{I\!P}(0) - \alpha' \cdot |t| \simeq 1.08 - 0.25 \cdot |t|$ (for t in GeV^2). For Q^2 larger than a few GeV^2, perturbative QCD (pQCD) is expected to apply and diffractive ρ production can be viewed in the proton rest frame as a sequence of three processes well separated in time : the photon fluctuation into a $q\bar{q}$ pair, the hard interaction of the $q\bar{q}$ pair with the proton via the exchange of two gluons in a net color-singlet state, and the $q\bar{q}$ pair recombination into a real ρ meson. The cross section is then proportional to the square of the gluon density in the proton, which corresponds to a fast increase of the $\gamma^* p$ cross section with the energy (“hard” behavior) [2].

Three angles are defined [3] to characterise the electroproduction of vector mesons (VM) decaying into two charged particles: Φ is the angle between the VM production plane (defined as the plane containing the virtual photon and the VM directions) and the electron scattering plane in the ($\gamma^\star p$) centre of mass system, θ^* and ϕ are the polar and the azimuthal angles, respectively, of the positively charged decay particle in the VM rest frame, the quantisation axis being taken as the direction opposite to that of the outgoing Y system. In this paper, the distributions of the angles Φ and θ^* are analysed.

2 Data selection and kinematics

2.1 Event selection

The data used for the present analysis were taken with the H1 detector in the year 2000. The energies of the HERA proton and positron beams [1] were 920 and 27.5 GeV, respectively. The data correspond to an integrated luminosity of 42.4 pb^{-1}.

---

[1] In the following, the word electron will be used for positrons.

The relevant parts of the detector, for which more details can be found in [4, 5], are the central tracking detector, the liquid argon (LAr) and the backward electromagnetic (SPACAL) calorimeters and the forward detectors, which are sensitive to energy flow close to the outgoing proton direction [2]. The forward detectors consist of the proton remnant tagger (PRT) made of a set of 7 scintillators surrounding the beam pipe 24 m downstream of the ep interaction point, and the three planes of the forward muon detector (FMD) situated between the interaction point and the solenoidal magnet.

Events candidates corresponding to reaction (1), in the kinematic range defined by relations (2) are selected by requesting :

- the reconstruction of a cluster in the SPACAL calorimeter with energy larger than 17 GeV (the scattered electron candidate);
- the reconstruction in the central tracking detector of the trajectories of exactly two charged particles (pion candidates) with opposite charges, transverse momenta larger than 0.1 GeV and polar angles confined within the interval $20^\text{o} < \theta < 160^\text{o}$;
- the invariant mass $M_{\pi\pi}$ of the decay pions to be $0.6 < M_{\pi\pi} < 1.1$ GeV;
- the absence of any energy deposit larger than 400 MeV in the LAr calorimeter not associated with the two charged pion candidates. This cut reduces backgrounds due to the diffractive production of systems decaying into two charged and additional neutral particles. It also helps to reject proton dissociative events with large M_Y masses;
- the absence of activity above noise in the PRT and the FMD, in order to reject events with proton dissociation;
- $M_{KK} > 1.04$ GeV, where M_{KK} is the invariant mass of the two pions candidates when considered as kaons (no direct hadron identification is performed for this analysis). This cut reduces the background due to diffractive production of ϕ mesons;
- $\sum(E - p_z) > 45$ GeV, to reduce both the effect of QED radiative corrections and background contributions in which there are unreconstructed particles. $\sum(E - p_z)$ is the difference of the energies and the longitudinal momenta of the scattered electron (measured in the SPACAL) and the pion candidates (measured in the central tracking detector). It is expected to be close to twice the incident electron beam energy, i.e. 55 GeV, if no other particles have been produced except for the forward going system Y, in particular if no high energy photons are radiated by the incoming or the outgoing electron.

To first approximation, the selected events can be attributed to elastic scattering. However, this sample also contains proton dissociative events either when the Y system has too small a mass to be detected ($M_Y \lesssim 1.6$ GeV), or due to inefficiencies of the forward detectors. Conversely, elastic events can be lost due to noise in the forward detectors or, for the highest $|t|$ values, when the scattered proton hits the beam pipe walls or adjacent material, leading to secondary particles which give a signal in the forward detectors.

---

[2] In the H1 convention, the z axis is defined by the colliding beams, the forward direction being that of the outgoing proton beam ($z > 0$) and the backward direction that of the electron beam ($z < 0$).

To estimate these backgrounds and losses, a "tag" sample is defined comprising the events which pass all of the cuts above, except that a signal is observed in the forward detectors. This sample mainly contains proton dissociation events, with $1.6 \lesssim M_Y \lesssim 5$ GeV, the upper bound on M_Y being due to the request of no energy deposit above noise in the LAr calorimeter.

The $\pi^+\pi^-$ mass distribution of the selected events is shown in fig. 1. A clear ρ meson signal is visible. The contributions from ω, ϕ and ρ' backgrounds extracted from Monte-Carlo simulations (see section 3.2) are also shown.

2.2 Kinematics

The three-momentum of the ρ is computed as the sum of the two charged pion candidate momenta. The variable Q^2 is reconstructed using the double angle method [6]:

$$Q^2 = \frac{4E_0^2 \, \sin\theta_\rho \, (1+\cos\theta_e)}{\sin\theta_e + \sin\theta_\rho - \sin(\theta_e+\theta_\rho)}, \tag{3}$$

where E_0 is the energy of the incoming electron and θ_e and θ_ρ are the scattered electron and ρ meson polar angles, respectively. The W variable is calculated using the Jacquet-Blondel method [7]:

$$W^2 = y \cdot s - \frac{{p_{t,\rho}}^2}{1-y}, \text{with } y = \frac{E_\rho - p_{z,\rho}}{2E_0}, \tag{4}$$

s being the square of the ep centre of mass energy and E_ρ, $p_{z,\rho}$ and $p_{t,\rho}$ being the energy, the longitudinal and the transverse momentum of the ρ meson, respectively. The variable $|t|$ is determined from the scattered electron and ρ momentum components transverse to the beam direction as

$$|t| \simeq (\vec{p}_{t,miss})^2 = (\vec{p}_{t,e} + \vec{p}_{t,\rho})^2, \tag{5}$$

where the electron transverse momentum is computed as

$$p_{t,e} = \frac{2E_0 - E_\rho + p_{z,\rho}}{\tan(\theta_e/2)} \; . \tag{6}$$

3 Monte Carlo simulations and backgrounds

3.1 Monte Carlo simulations

A Monte Carlo program based on the DIFFVM program [8] including QED radiation [9] simulates the elastic production and the decay of ρ vector meson. It is used to correct the data for acceptance, smearing and radiative effects. The Q^2, W and t dependences of the cross section, including their correlations, are taken from the present measurements (see figs. 3, 5 and 7). The simulation includes the angular distributions corresponding to the measurements of the present analysis for the r^{04}_{00} matrix element ($\cos\theta^*$ distribution) and for the $r^5_{00} + 2r^5_{11}$ and $r^1_{00} + 2r^1_{11}$ combinations (Φ distribution), combined in the latter case with the measurements in [10]. Other angular distributions and correlations are taken in the s-channel helicity conservation (SCHC) approximation, and the $\cos\delta$ parameter, which describes the interference between the longitudinal and transverse amplitudes, is taken from the measurement from [11] in the relevant Q^2 range. The mass distribution is described by a relativistic Breit-Wigner distribution, including skewing effects taken from [11]. For studies of systematic errors all the simulation parameters have been varied within errors.

DIFFVM is also used for the simulation of the ρ proton dissociative background, and of ω, ϕ and ρ' backgrounds. For the proton dissociative ρ background, the slope of the exponential t dependence is taken to be 1.7 GeV^{-2}, a value determined from the present data using the “tag” sample. The angular distributions are assumed to be the same as for elastic ρ case, and the M_Y spectrum is parameterised as $\mathrm{d}\sigma/\mathrm{d}M_Y^2 \propto 1/M_Y^{2.15}$ (see [12]). The slope of the t distribution is taken to be 6 GeV^{-2} for elastic ω, ϕ and ρ' production.

Fig. 2 shows various distributions, comparing the data sample with the Monte Carlo simulation. The background discussed in section 3.2 are also shown. Good agreement is observed for all distributions, indicating that the Monte-Carlo simulations can be reliably used to correct the data for acceptance and smearing effects.

3.2 Proton dissociative ρ and ω, ϕ and ρ' backgrounds

A proton dissociative background of $11 \pm 4\%$ is estimated using the number of events in the selected sample and in the “tag” sample, and the probabilities of no signal in the PRT and the FMD for elastic and proton dissociative ρ events, respectively. The error reflects the statistical precision of the data and the systematic uncertainties determined by varying the conditions imposed on the forward detectors, by varying the proton dissociative t slope by $\pm 0.5\ \mathrm{GeV}^{-2}$ and by varying the M_Y^2 spectrum from $1/M_Y^{2.15}$ to $1/M_Y^{1.85}$ and to $1/M_Y^{2.45}$

Diffractive electroproduction of ω and ϕ mesons can fake ρ production through the decay channels:

$$\begin{aligned}
&\omega \to \pi^+\pi^-\pi^0, \\
&\phi \to \pi^+\pi^-\pi^0, \qquad \phi \to K_S^0 K_L^0, \\
&\rho' \to \rho^+\pi^-\pi^0, \qquad \rho^+ \to \pi^+\pi^0 \qquad (+\,c.c.).
\end{aligned} \tag{7}$$

if the decay photons of the π^0 or the K_L^0 mesons are not detected. Diffractive electroproduction of ω and ϕ mesons also gives the same topology in the detector as for ρ production through the decay channels

$$\begin{aligned}
&\omega \to \pi^+\pi^-, \\
&\phi \to \mathrm{K}^+\mathrm{K}^-.
\end{aligned} \tag{8}$$

The ω, ϕ and ρ' cross sections were taken from measured ratios to the ρ cross section, in the Q^2 range relevant for the analysis: ω / $\rho = 0.09$ [14], ϕ / $\rho = 0.20$ [13] and ρ' / $\rho = 1.00$ (compatible with the analysis in [10]).

The background contributions in the selected kinematic domain (2) and for the selected ρ mass range are estimated with Monte-Carlo simulations The total remaining amount of background is 0.35 % for ω, 0.25 % for ϕ and 4 % for ρ'. These contributions are subtracted from all experimental distributions.

4 Cross sections

In each bin of the kinematical variables Q^2 and W, the cross section is computed from the numbers of events in the bin, fully corrected for background, acceptance, smearing and QED radiation effects using the Monte Carlo simulations described above. It is converted into a $\gamma^* p$ cross section using the relation:

$$\frac{\mathrm{d}^2\sigma_{tot}(ep \to e\rho p)}{\mathrm{d}y\,\mathrm{d}Q^2} = \Gamma\ \sigma_{tot}(\gamma^* p \to Vp) = \ \Gamma\ \sigma_T(\gamma^* p \to \rho p)\ (1 + \varepsilon\ R), \tag{9}$$

where σ_{tot}, σ_T and σ_L are the total, transverse and longitudinal $\gamma^* p$ cross sections and

$$R\ = \sigma_L/\sigma_T. \tag{10}$$

The flux Γ of transverse virtual photons given by

$$\Gamma = \frac{\alpha_{em}\ (1 - y + y^2/2)}{\pi\ y\ Q^2}; \tag{11}$$

and ε is the polarisation parameter

$$\varepsilon = \frac{1-y}{1 - y + y^2/2}. \tag{12}$$

For this analysis, $<\varepsilon>= 0.996$ ($0.93 < \varepsilon < 1$). The Q^2 and W dependences measured in the present analysis are taken into account in the computation of the flux factors.

The mass distributions were corrected for the analysis cut, to the range $2m_\pi < M_{\pi\pi} < m_\rho + 5\Gamma_\rho$, where m_π and m_ρ are the pion and ρ meson masses, respectively and Γ_ρ is the natural width of the ρ meson.

4.1 Q^2 dependence of the $\gamma^* p$ cross section

Fig. 3 shows the Q^2 dependence of the total $\gamma^* p$ cross section, for $W = 95$ GeV. A fit of the form $\sigma \propto 1/(Q^2 + m_\rho^2)^n$ for the range $8 < Q^2 < 60\ \mathrm{GeV}^2$ results in $n = 2.60 \pm 0.04$, with $\chi^2/ndf = 4.6/10$. Previous measurements [11, 15], extrapolated to $W = 95$ GeV, are also shown. Comparing the extracted value of n with the result $n = 2.24 \pm 0.09$ obtained from a sample [11] extending to lower $Q^2 > 1\ \mathrm{GeV}^2$, it is clear that this parameterisation is not sufficient to describe the sum of transverse and longitudinal photon induced cross sections for all Q^2.

4.2 W dependence of the $\gamma^* p$ cross section

Fig. 4 shows the W dependence of the $\gamma^* p$ cross section, at four values of Q^2. The rise of the cross section with W is observed to become stronger as Q^2 increases. Parameterising the W dependence at fixed Q^2 as $\sigma(W) \propto W^\delta$, the fitted values of δ are shown in fig. 5, together with previous measurements [11, 16]. Values similar to those for J/ψ photoproduction [17] are reached at the highest Q^2 values, suggesting similarly hard production mechanisms for ρ electroproduction at high Q^2 and J/ψ photoproduction.

4.3 t dependence

The t dependence of the cross section is shown in fig. 6, for four intervals in Q^2. The superimposed curves show the results of fits to exponential parameterisations $\mathrm{d}\sigma/\mathrm{d}t \propto \exp{(bt)}$. The slopes b are shown as a function of Q^2 in fig. 7, together with previous measurements [11, 18, 15]. As Q^2 increases, the b slopes decrease, reflecting the decrease of the transverse size of the $q\bar{q}$ pair into which the photon fluctuates as Q^2 increases. At the largest Q^2 the b parameter is compatible with that obtained in J/ψ photoproduction [17] and is close to the value expected from the proton form factor.

4.4 r_{00}^{04} spin density matrix element

Fig. 8 shows the $\cos\theta^*$ dependence of the cross section, for three intervals in Q^2, three intervals in W and three intervals in t. The superimposed curves show the results of fits of the form

$$\frac{\mathrm{d}\sigma}{\mathrm{d}\cos\theta^*} \propto 1 - r_{00}^{04} \ + (3\, r_{00}^{04} - 1)\cos^2\theta^*. \tag{13}$$

The extracted values of the r_{00}^{04} spin density matrix element are shown in fig. 9 as a function of Q^2, W and t.

The r_{00}^{04} matrix element grows with Q^2, indicating a significant increase of the longitudinal to transverse cross section ratio, up to the highest accessible Q^2 values. Fig. 10 shows the corresponding value of $R = \sigma_L/\sigma_T$ together with previous measurements [11, 18, 19, 15]. R is detemined under the approximation of s-channel helicity conservation using the relation

$$R = \frac{1}{\varepsilon}\frac{r_{00}^{04}}{(1 - r_{00}^{04})}. \tag{14}$$

The Q^2 dependence of R is well described by the model of Martin, Ryskin and Teubner [20], based on parton-hadron duality, using the MRS(R4) [21] parton densities.

With the present precision, there is no evidence for any dependence of r_{00}^{04} on W or t. The lack of t dependence indicates that, in the measured range, the longitudinal and transverse cross sections have very similar t dependences.

4.5 $(r_{00}^{5} + 2r_{11}^{5})$ and $(r_{00}^{1} + 2r_{11}^{1})$ combinations

Fig. 11 shows the Φ dependence of the cross section, for three intervals in Q^2, three intervals in W and three intervals in t. The superimposed curves show results of fits of the form

$$\frac{\mathrm{d}\sigma}{\mathrm{d}\Phi} \propto 1 + \sqrt{2\varepsilon(1+\varepsilon)}\ \cos\Phi\ (r_{00}^{5} + 2r_{11}^{5}) - \varepsilon\ \cos 2\Phi\ (r_{00}^{1} + 2r_{11}^{1}), \tag{15}$$

where the spin density matrix element combinations $r_{00}^{5} + 2r_{11}^{5}$ and $r_{00}^{1} + 2r_{11}^{1}$ are sensitive to the transition amplitudes in which the helicity of the ρ meson is different from that of the virtual photon [10].

The extracted combinations of spin density matrix elements $r^5_{00} + 2r^5_{11}$ and $r^1_{00} + 2r^1_{11}$ are shown as a function of Q^2, W and $|t|$ in figs. 12 and 13, respectively. Values significantly different from zero and increasing with $|t|$ are obtained for the $r^5_{00} + 2r^5_{11}$ combination, confirming s-channel helicity non conservation [11, 10, 22] as predicted by pQCD based models [23, 24]. At the largest values of $|t|$ accessed, there is also an indication that the combination $r^1_{00} + 2r^1_{11}$ becomes negative. There is no evidence from the present data for any variation of the $r^5_{00} + 2r^5_{11}$ or $r^1_{00} + 2r^1_{11}$ combinations with Q^2 or W.

5 Conclusions

The elastic electroproduction of ρ mesons, $e + p \to e + \rho + p$, has been studied at HERA in the kinematic range $8 < Q^2 < 60 \text{ GeV}^2$, $40 < W < 180$ GeV, $0 < |t| < 0.5 \text{ GeV}^2$.

The Q^2, W and t dependences of the $\gamma^* p \to \rho p$ cross section have been measured. In the present Q^2 range, the Q^2 distribution is described by the form $\mathrm{d}\sigma/\mathrm{d}Q^2 \propto 1/(Q^2 + m^2_\rho)^n$, with $n = 2.60 \pm 0.04$. This value of n is significantly larger than that obtained when lower Q^2 data are included [11]. The W dependence of the cross section at fixed Q^2, when parameterised as $\sigma(W) \propto W^\delta$, confirms a significant increase of the fitted values of δ with Q^2. At the highest Q^2 , δ reaches values similar to that obtained in J/ψ photoproduction. Exponential fits to the $|t|$ dependence of the cross section give slope parameters b decreasing with increasing Q^2. For the highest Q^2 data, the slope parameter reaches values similar to those obtained for J/ψ photoproduction.

The r^{04}_{00} spin density matrix element and the combinations $r^5_{00} + 2r^5_{11}$ and $r^1_{00} + 2r^1_{11}$ have been measured as a function of Q^2, W and $|t|$. The r^{04}_{00} spin density matrix element increases with Q^2, indicating a significant increase of the longitudinal to transverse cross section ratio, up to the highest available Q^2 values. In contrast, with the present precision, r^{04}_{00} is independent of W and $|t|$. The latter feature indicates that, in the measured range, the longitudinal and transverse cross sections have similar $|t|$ dependences. Values significantly different from zero and increasing with $|t|$ are obtained for the $r^5_{00} + 2r^5_{11}$ matrix element combination, confirming s-channel helicity non-conservation [11, 10, 22].

Acknowledgements

We are grateful to the HERA machine group whose outstanding efforts have made and continue to make this experiment possible. We thank the engineers and technicians for their work in constructing and now maintaining the H1 detector, our funding agencies for financial support, the DESY technical staff for continual assistance, and the DESY directorate for the hospitality which they extend to the non DESY members of the collaboration.

References

[1] A. Donnachie and P.V. Landshoff, Phys. Lett. **B395** (1997) 311.

[2] M.G. Ryskin *et al.*, Z. Phys. **C76** (1997) 231.

[3] K. Schilling and G. Wolf, Nucl. Phys. **B61** (1973) 381.

[4] I. Abt *et al.* [H1 Collaboration], Nucl. Instrum. Meth. A **386** (1997) 310.

[5] R. D. Appuhn *et al.* [H1 SPACAL Group], Nucl. Instrum. Meth. A **386** (1997) 397.

[6] S. Bentvelsen, J. Engelen and P. Kooijman, in Proc. of the Workshop on Physics at HERA, W. Buchmüller and G. Ingelman ed., Hamburg (1992) 23; K.C. Hoeger, ibid, p 43.

[7] F. Jacquet and A. Blondel, DESY 79-048 (1979) 377.

[8] B. List and A. Mastroberardino, in Proc. of the Workshop on Monte Carlo Generators for HERA Physics, A.T. Doyle et al. ed., DESY-PROC-1999-02 (1999) 396.

[9] A. Kwiatkowski, H.-J. Möhring and H. Spiesberger, Comput. Phys. Commun. **69** (1992), 155 and Proc. of the Workshop on Physics at HERA, W. Buchmüller and G. Ingelman ed., Hamburg (1992) 1294.

[10] C. Adloff *et al.* [H1 Collaboration], “ A measurement of the t dependence of the helicity structure of diffractive ρ meson electroproduction at HERA”, accepted by Phys Lett. B [hep-ex/0203022].

[11] C. Adloff *et al.* [H1 Collaboration], Eur. Phys. J. **C13** (2000) 371.

[12] K. Goulianos, Phys. Rep. **101** (1983) 169.

[13] C. Adloff *et al.* [H1 Collaboration], Phys. Lett. **B483** (2000) 360.

[14] J. Breitweg *et al.* [ZEUS Collaboration], Phys. Lett. **B487** (2000) 273.

[15] J. Breitweg *et al.* [ZEUS Collaboration], Eur. Phys. J. **C6** (1999) 603.

[16] ZEUS Collaboration, “Exclusive electroproduction of ρ^0 mesons at HERA”, Contrib. pap. 594 to the Eur. Phys. Soc. Conference, Budapest 2001.

[17] C. Adloff *et al.* [H1 Collaboration], Phys. Lett. **B483** (2000) 23.

[18] S. Aid *et al.* [H1 Collaboration], Nucl. Phys. **B463** (1996) 3.

[19] J. Breitweg *et al.*, [ZEUS Collaboration], Eur. Phys. J. **C2** (1998) 247.

[20] A. Martin, M. Ryskin, T. Teubner, Phys. Rev. **D55** (1997) 4329.

[21] A. Martin, R. Roberts, W. Stirling, Phys. Lett. **B387** (1986) 419.

[22] J. Breitweg *et al.* [ZEUS Collaboration], Eur. Phys. J. **C12** (2000) 393.

[23] D.Yu. Ivanov and R. Kirschner, Phys. Rev. **D58** (1998) 114026.

[24] E.V. Kuraev, N.N. Nikolaev and B.G. Zakharov, JETP Lett. **68** (1998) 696.

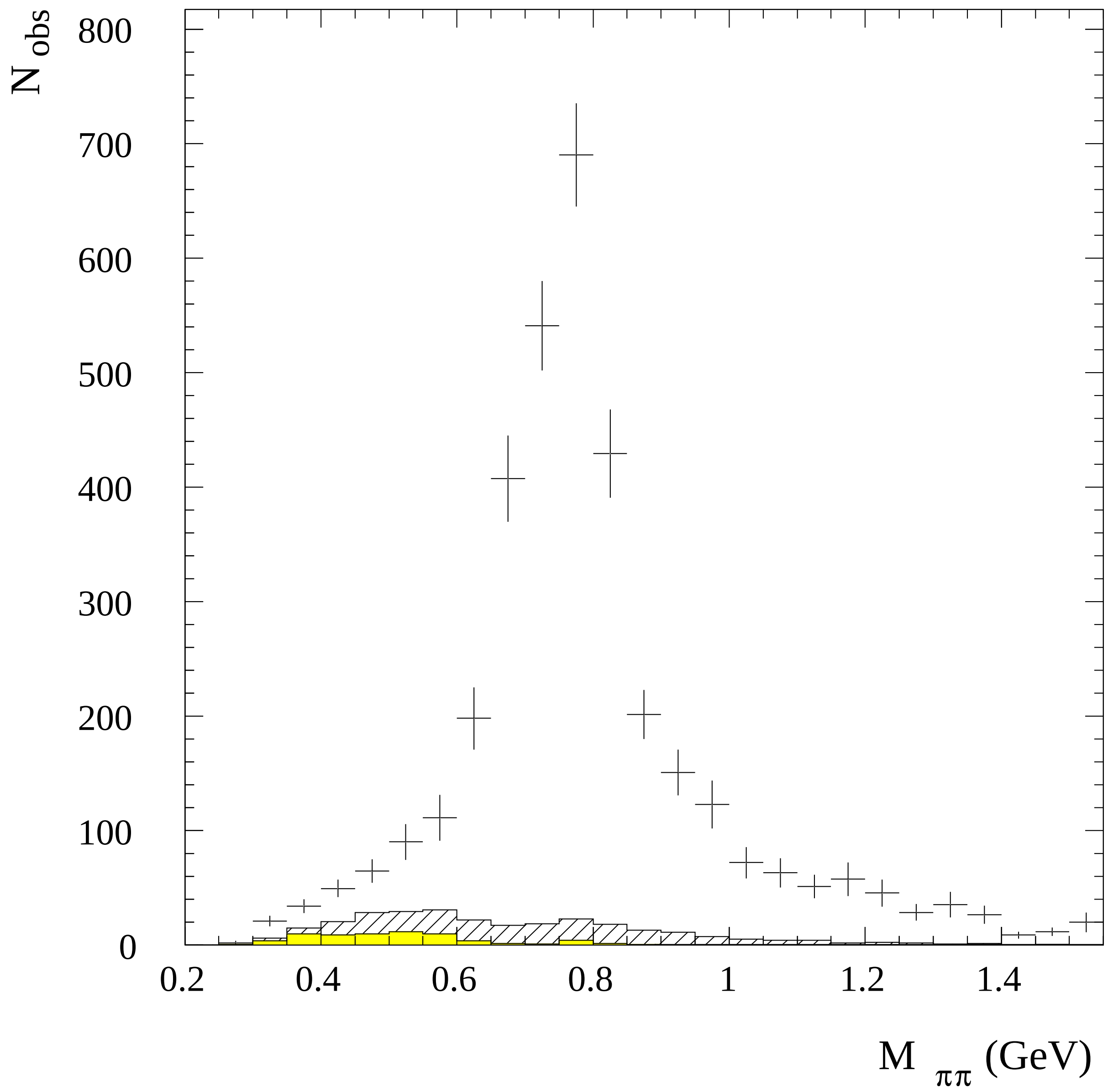

Figure 1: Uncorrected $\pi^+\pi^-$ mass distribution for the selected events with $0.3 < M_{\pi\pi} < 1.5$ GeV; the shaded histograms show the ω and ϕ backgrounds and the hatched histograms the ρ' background.

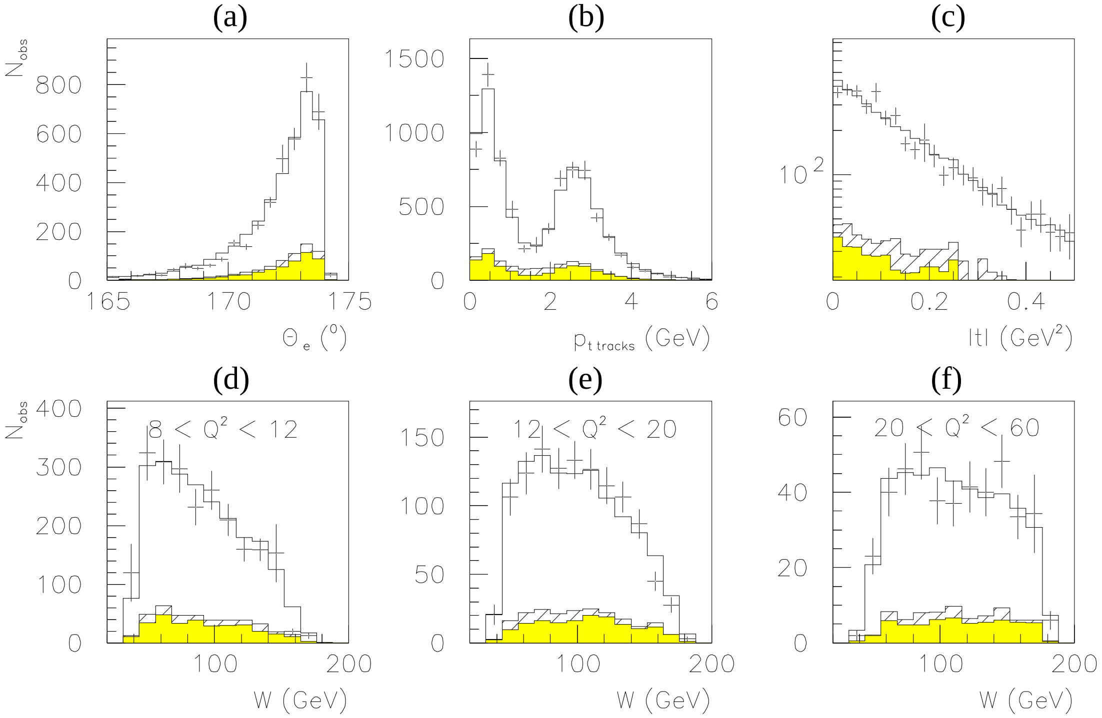

Figure 2: Distribution of the selected events in the kinematic domain (2) and in the mass range $0.6 < M_{\pi\pi} < 1.1$ GeV, for the scattered electron polar angle (a), the pion candidate transverse momentum p_t (b), $|t|$ (c), W for $8 < Q^2 < 12$ GeV^2 (d), $12 < Q^2 < 20$ GeV^2 (e) and $20 < Q^2 < 60$ GeV^2 (f). The histograms show the Monte-Carlo predictions, including the proton dissociative (shaded histograms) and the ω, ϕ and ρ' backgrounds (hatched histograms).

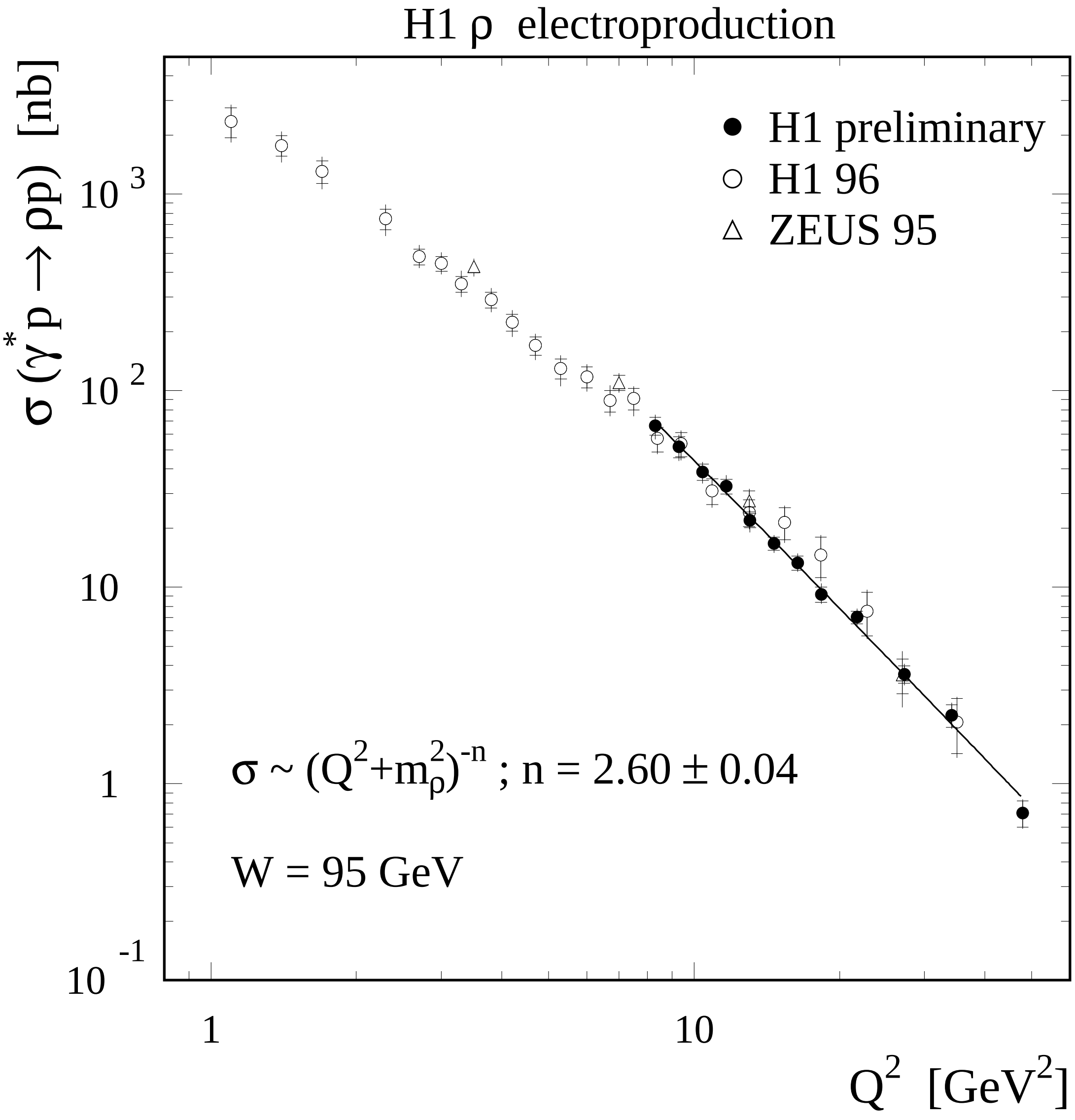

Figure 3: The $\gamma^* p \rightarrow \rho p$ cross section as a function of Q^2, for $W = 95$ GeV. Also shown are the data from [11, 15], extrapolated to the same W value using the W dependence measured in the present analysis. The inner error bars are statistical, and the full error bars include the systematic errors added in quadrature. The superimposed line is for $\sigma \propto 1/(Q^2 + m_\rho^2)^n$ with $n = 2.60$. The fit error includes both statistical and uncorrelated systematic errors.

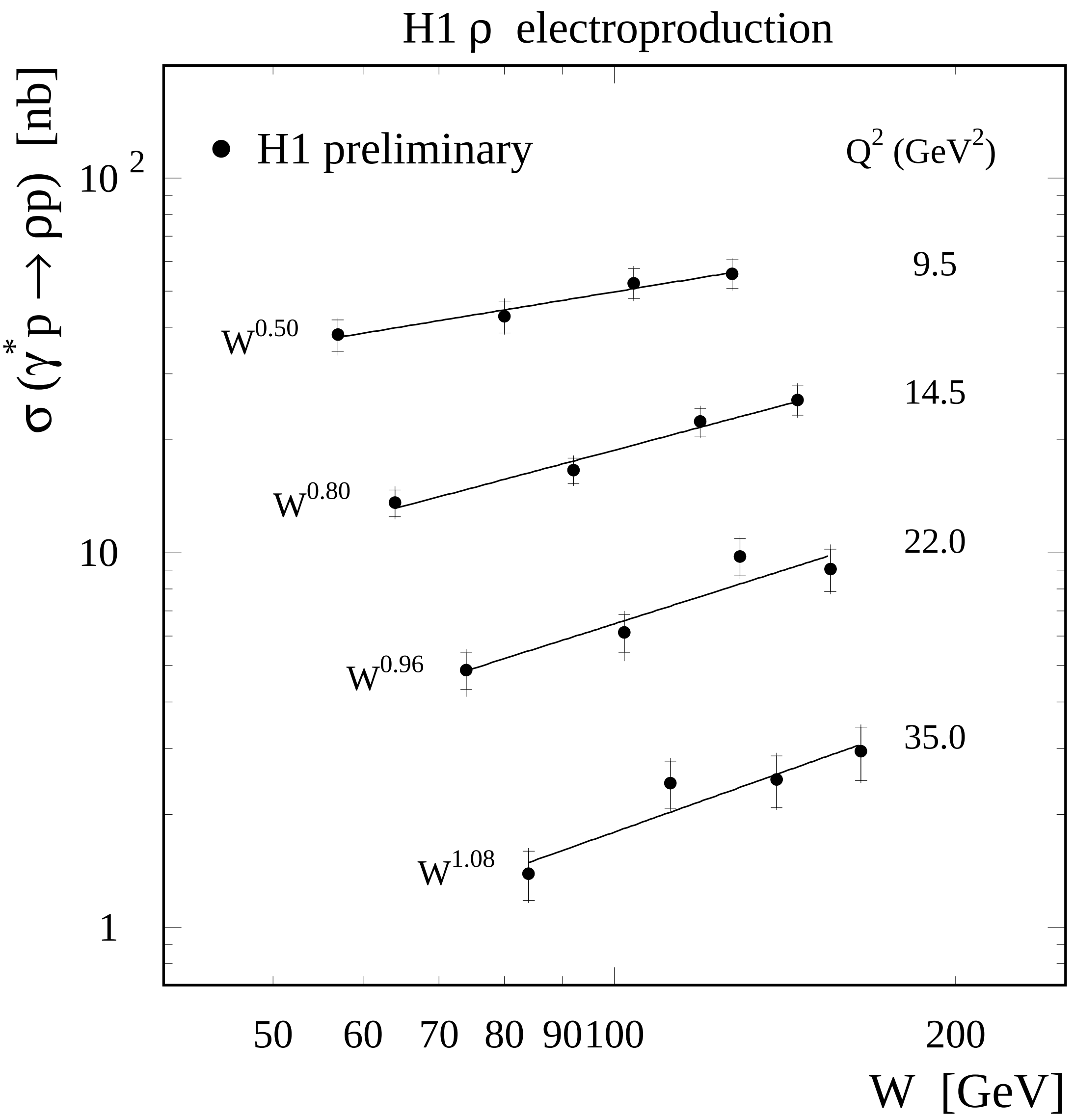

Figure 4: The $\gamma^* p \to \rho p$ cross section as a function of W for several Q^2 values. The inner error bars are statistical, and the full error bars include the systematic errors added in quadrature. The superimposed lines represent parameterisations of the form $\sigma(W) \propto W^\delta$.

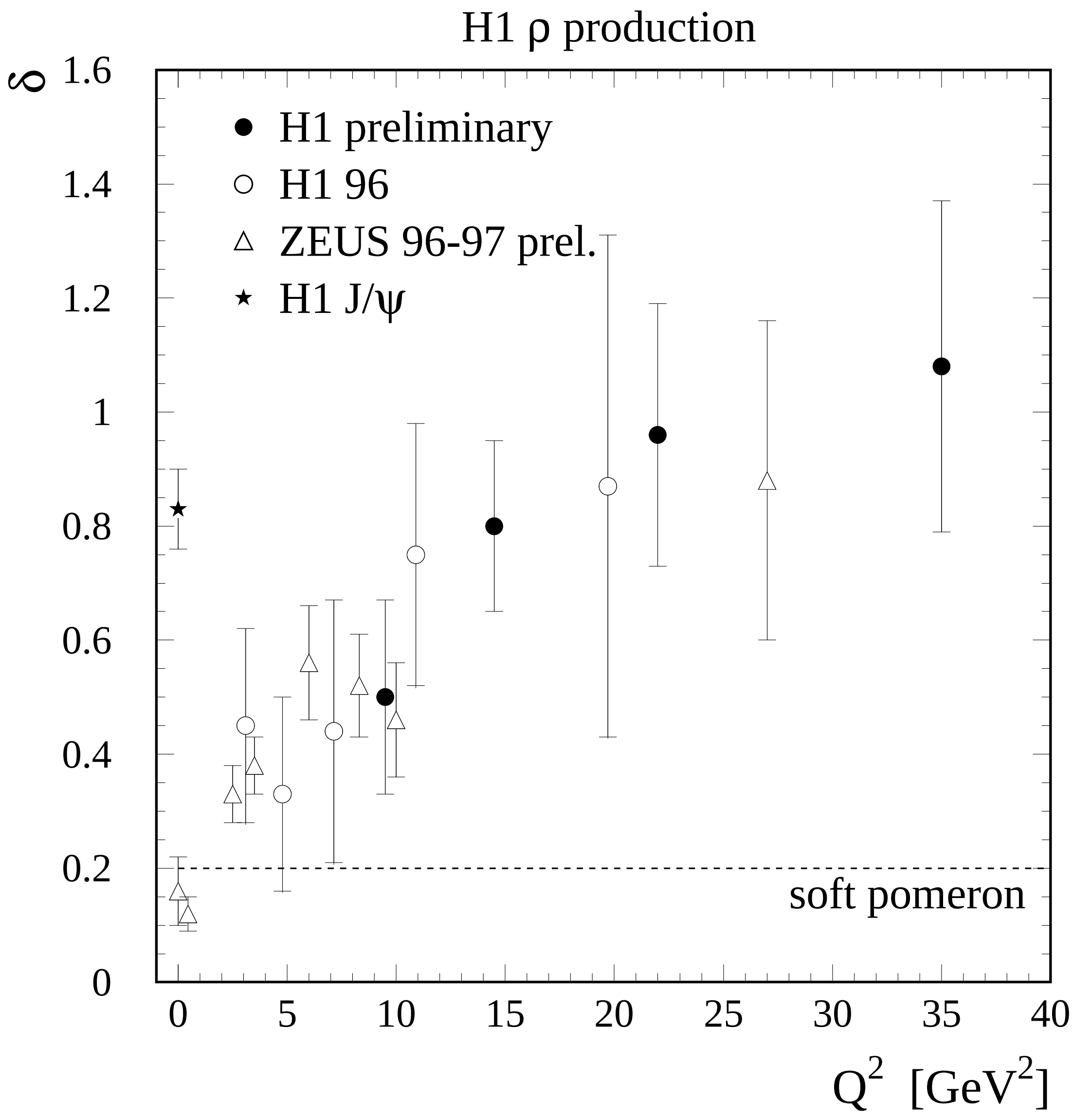

Figure 5: Results of fits of the form $\sigma(W) \propto W^{\delta}$ to the W dependence of the $\gamma^{*}p$ cross section, presented as a function of Q^2. Also shown are the measurements [11] and [16] for ρ meson production and [17] for J/ψ photoproduction. The errors include both statistical and uncorrelated systematic errors.

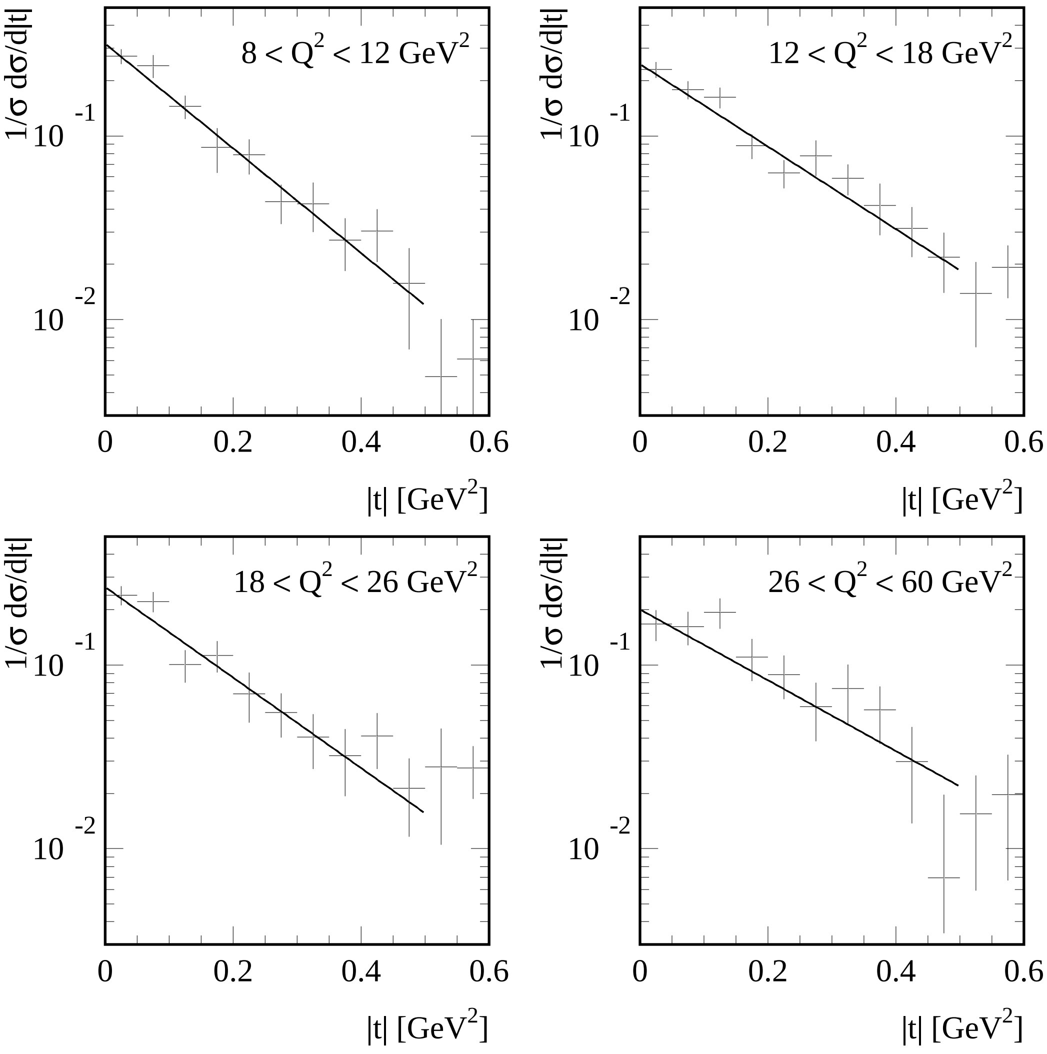

Figure 6: The $|t|$ dependence of the cross section, for several Q^2 intervals. The superimposed curves show results of fits to exponential distributions for $|t| < 0.5\ \mathrm{GeV}^2$. Only the statistical errors are shown.

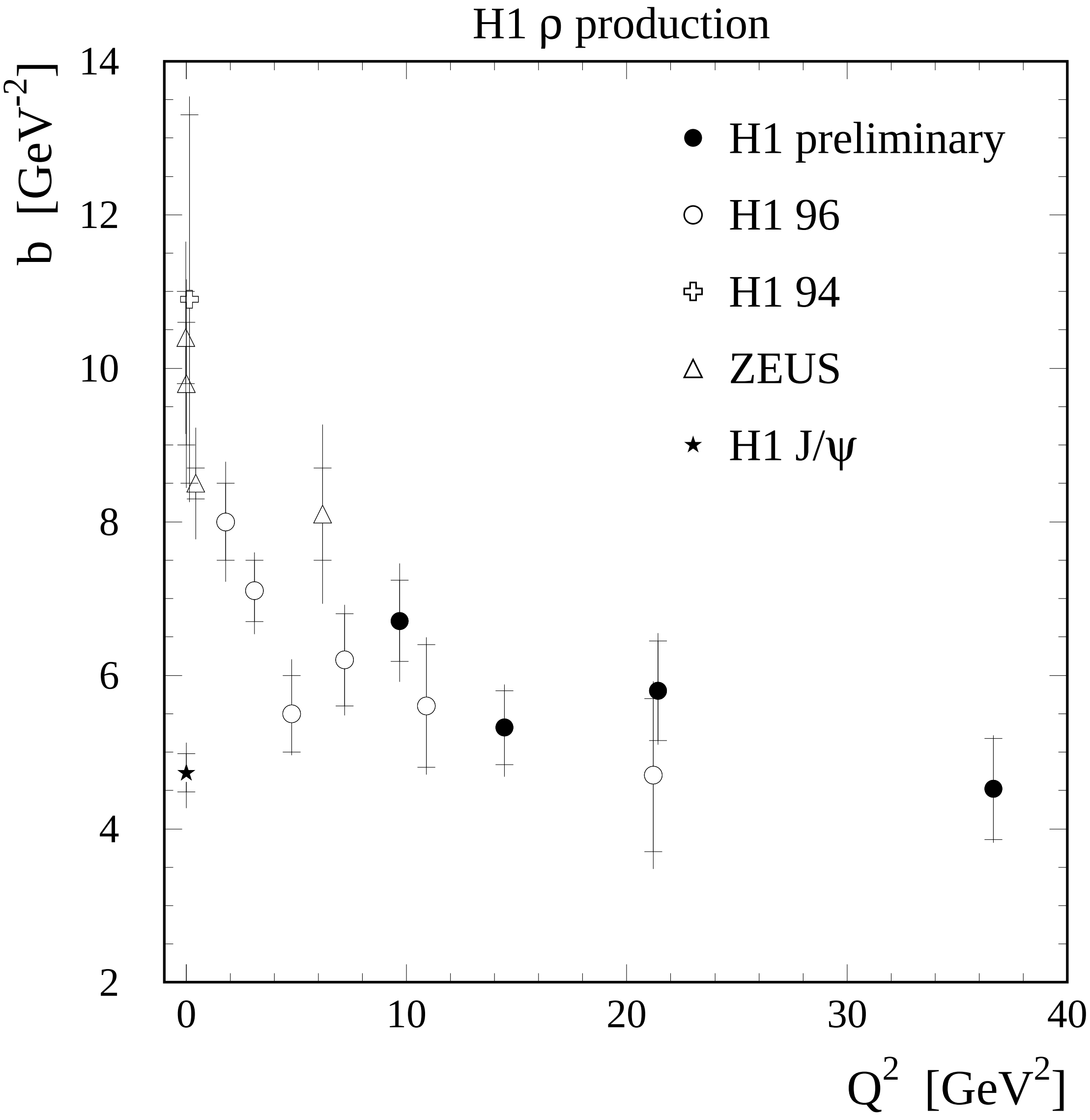

Figure 7: Results of fits to an exponential parameterisation of the $|t|$ dependence of the cross section, presented as a function of Q^2. Also shown are the measurements [11], [18] and [15] for ρ meson production and [17] for J/ψ photoproduction. The inner error bars are statistical, and the full error bars include the systematic errors added in quadrature.

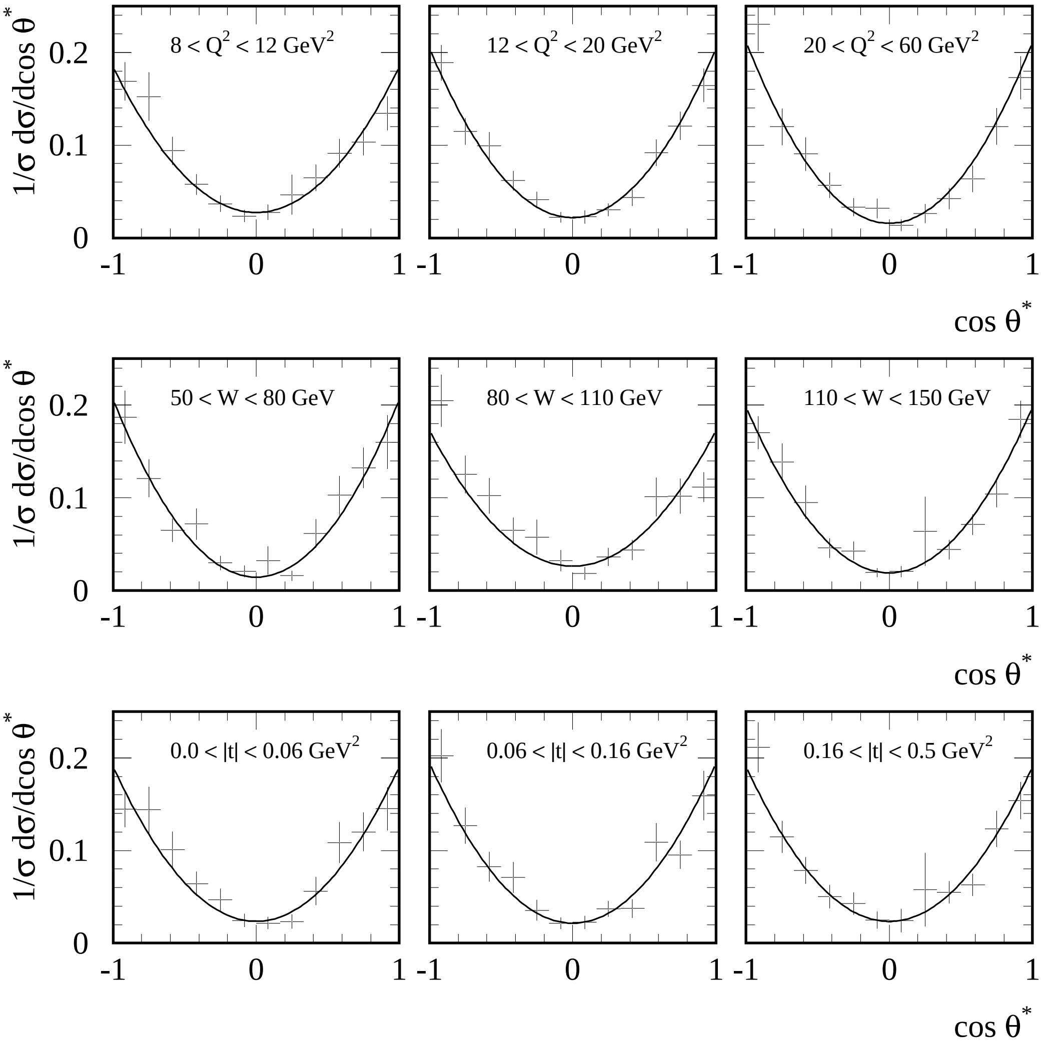

Figure 8: The $\cos\theta^*$ dependence of the cross section, for severals Q^2, W and $|t|$ intervals. The superimposed curves show results of fits to the relation (13).

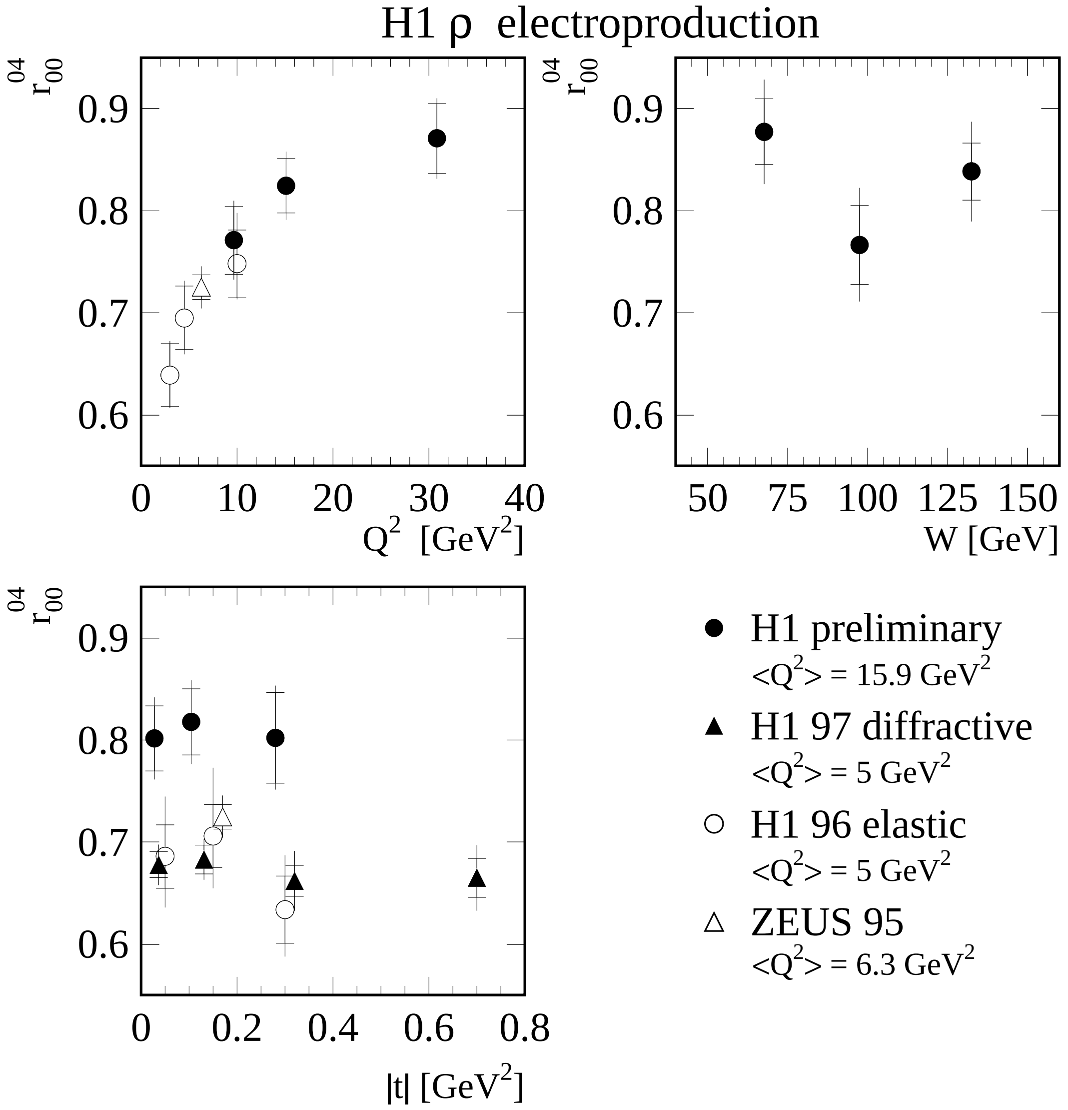

Figure 9: Measurements of the r_{00}^{04} spin density matrix element, as a function of Q^2, W and $|t|$. Also shown are the measurements [11, 10, 22]. The data labelled "H1 97 diffractive" correspond to measurements without separation of the elastic and the proton dissociative channels. The inner error bars are statistical, and the full error bars include the systematic errors added in quadrature.

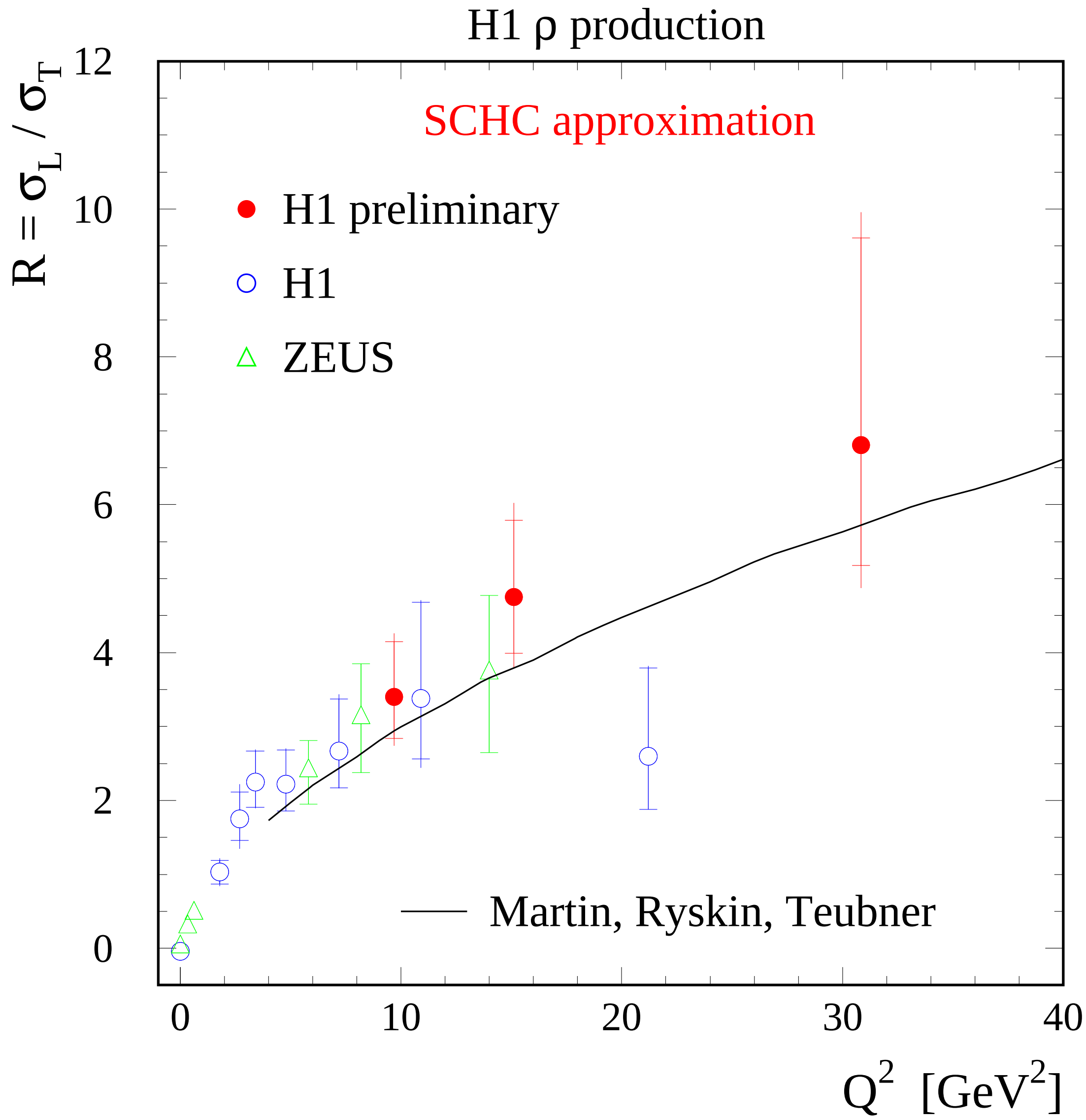

Figure 10: The ratio R of longitudinal to transverse cross sections for elastic ρ meson electroproduction by longitudinal and transverse photons, measured in the SCHC approximation and presented as a function of Q^2. The other measurements are from H1 [11, 18] and ZEUS [19, 15]. The inner error bars are statistical, and the full error bars include the systematic errors added in quadrature. The line corresponds to the prediction of Martin, Ryskin and Teubner [20].

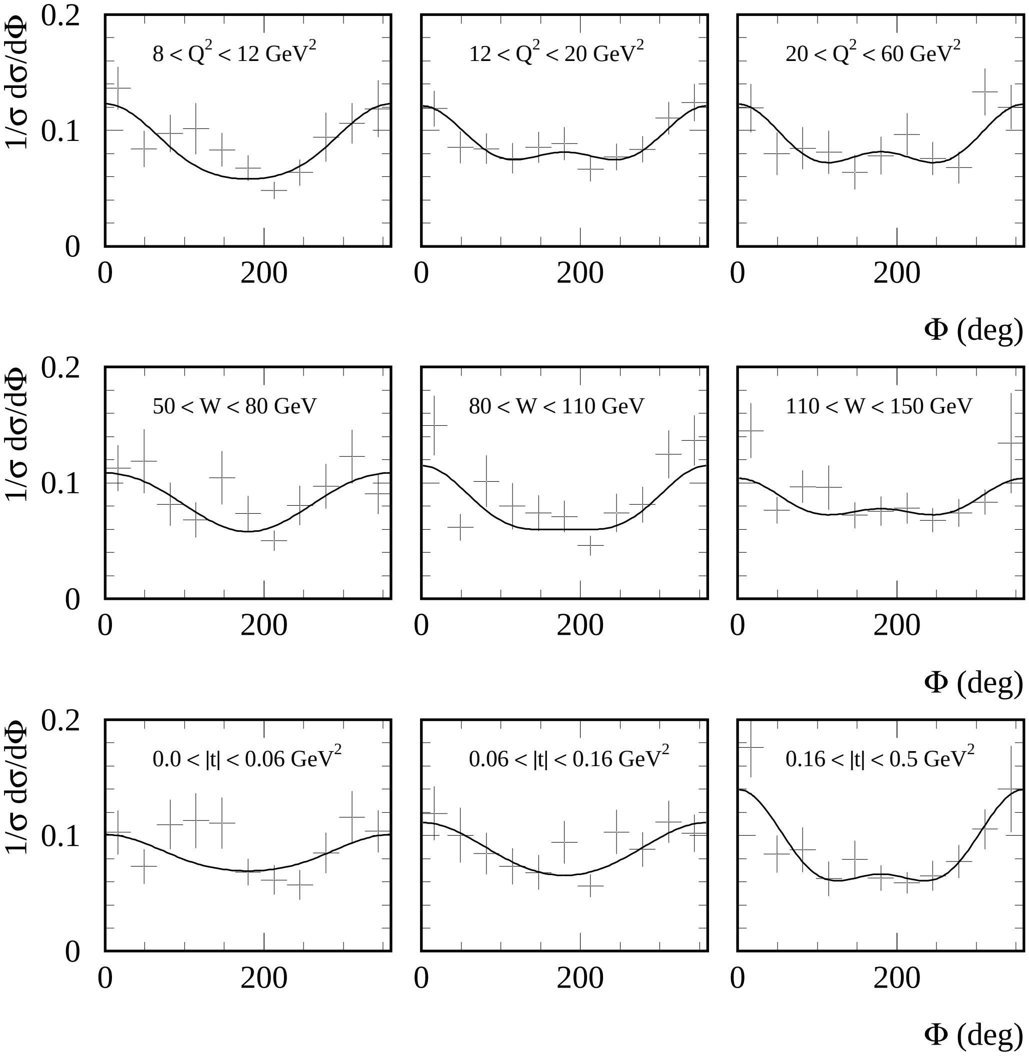

Figure 11: The Φ dependence of the cross section, for severals Q^2, W and $|t|$ intervals. The superimposed curves show results of fits to the relation (15).

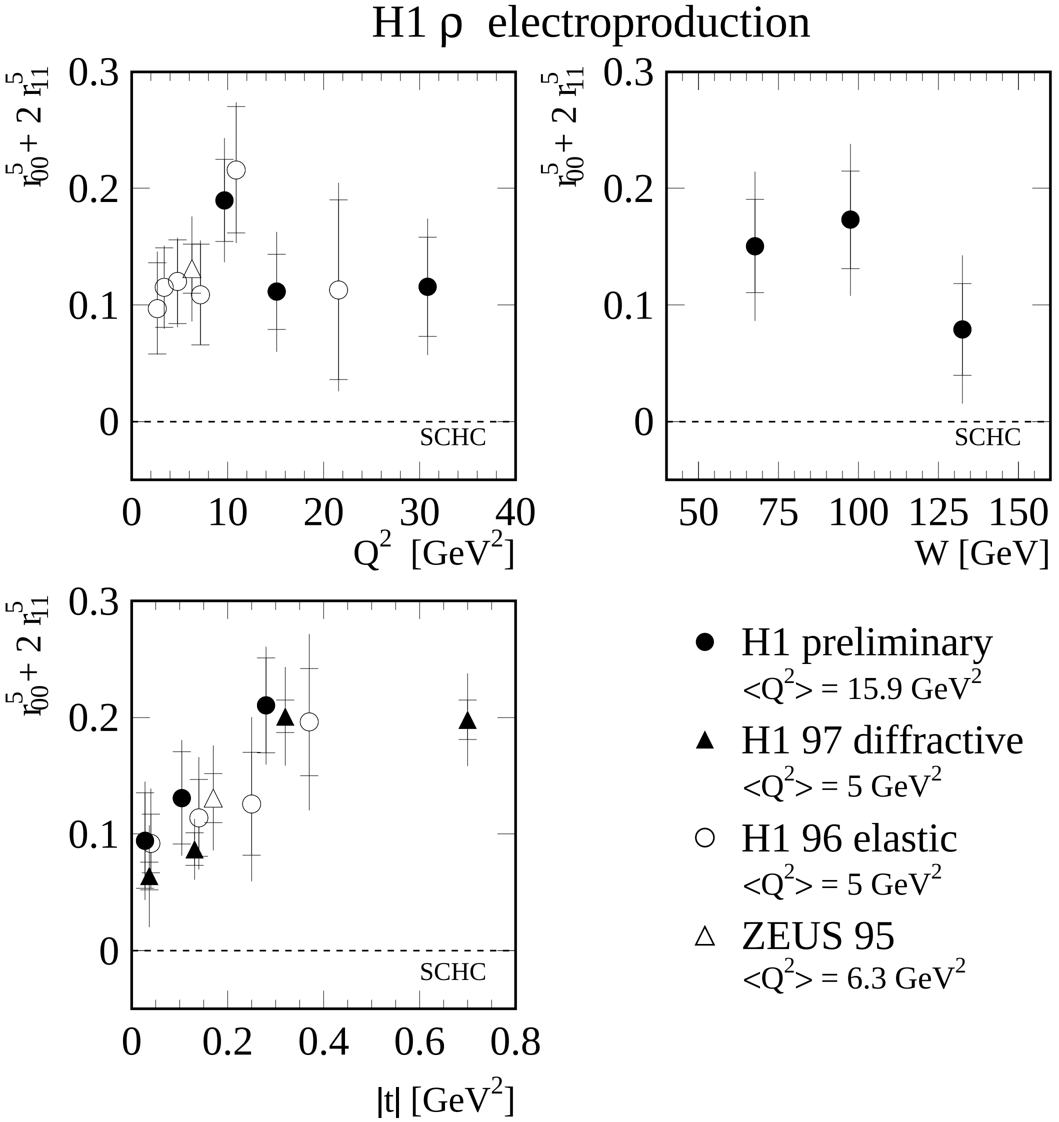

Figure 12: Measurements of the $r^5_{00} + 2r^5_{11}$ spin density matrix element combination as a function of Q^2, W and $|t|$. Also shown are the measurements [11, 10, 22]. The inner error bars are statistical, and the full error bars include the systematic errors added in quadrature. The dashed lines indicate the expected null values in the case of s-channel helicity conservation (SCHC).

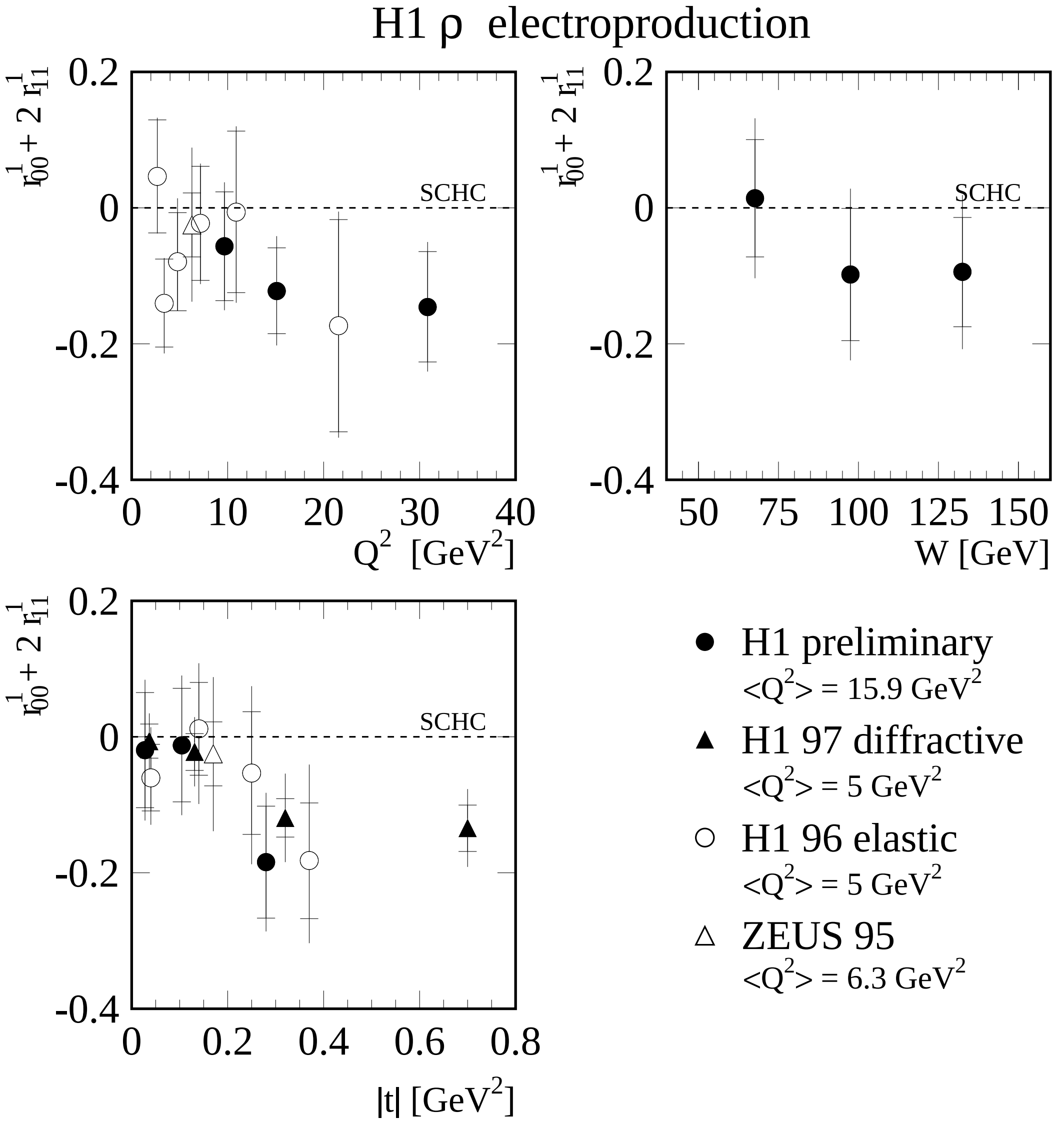

Figure 13: Measurements of the $r^1_{00} + 2r^1_{11}$spin density matrix element combination as a function of Q^2, W and $|t|$. Also shown are the measurements [11, 10, 22]. The inner error bars are statistical, and the full error bars include the systematic errors added in quadrature. The dashed lines indicate the expected null values in the case of s-channel helicity conservation (SCHC).